

**Structural and spectroscopic comparison between polycrystalline,  
nanocrystalline and quantum dot visible light photo-catalyst**



Michael Teck<sup>a,e</sup>, M. Mangir Murshed<sup>a,e\*</sup>, Marco Schowalter<sup>b,e</sup>, Niels Lefeld<sup>a,e</sup>, Henrike K. Grossmann<sup>c,e</sup>, Tim Grieb<sup>b,c,e</sup>, Thomas Hartmann<sup>d</sup>, Lars Robben<sup>a,e</sup>, Andreas Rosenauer<sup>b,e</sup>, Lutz Mädler<sup>c,e</sup>, Thorsten M. Gesing<sup>a,e</sup>

<sup>a</sup>Institute of Inorganic Chemistry and Crystallography, University of Bremen, Leobener Str. /NW2, 28359 Bremen, Germany

<sup>b</sup>Institute of Solid State Physics, University of Bremen, Otto-Hahn-Allee /NW1, D-28359 Bremen, Germany

<sup>c</sup>Foundation Institute of Materials Science (IWT), Department of Production Engineering, University of Bremen, Badgasteiner Strasse 3, 28359 Bremen, Germany

<sup>d</sup>Stoe & Cie GmbH, Hilpertstraße 10, 64295 Darmstadt, Germany

<sup>e</sup>MAPEX center for materials and processes, University of Bremen, Bibliothekstraße 1, 28359 Bremen, Germany

\*Corresponding author: e-mail address: murshed@uni-bremen.de, phone: +49 (0)421 218 63144, fax: +49 421 218 63145.

## **Abstract**

The structural and spectroscopic features of the visible light photocatalyst  $\text{Bi}_2\text{WO}_6$  have been studied. Polycrystalline (PC), nanocrystalline (NC) and quantum dot (QD) sized samples were produced using solid state reaction, hydrothermal and flame spray pyrolysis methods, respectively. While the crystal structures of PC and NC are well characterized using X-ray powder diffraction data Rietveld refinement, the structural information of the QD are obtained from the complementary pair distribution function analysis and high-resolution transmission electron microscopy. The Raman spectra of the samples are compared with the phonon density of states calculated by DFT. A continuous phenomenological model describes selective optical phonon confinement into the QDs. The type of the electronic bandgaps obtained from the UV-VIS absorbance-spectra have been analyzed using two different methods, and compared with those calculated from the electronic band structures.

**Keywords:** bismuth tungstate, X-ray diffraction, pair distribution function, Raman, UV-VIS, HRTEM, DFT.

## **1. Introduction**

Globally the pressing need of clean, economical and emission free energy as a replacement of fossil fuel stands beyond any further discussion. To meet the ever increasing demand the development and usage of heterogeneous photocatalysis is suggested to be one of the green energy approaches [1]. In this regard, advanced oxidation process such as water splitting [2] and decomposition of the pollutants in air and water [3][4][5] may play significant roles. Since the discovery of the photocatalytic splitting of water on TiO<sub>2</sub> electrodes [6] the usage of irradiated semiconductors for photocatalysis has been the subject of intensive studies [7][8][9]. Single polymorph of polycrystalline TiO<sub>2</sub>, their all possible mixtures [10] and nanocrystalline TiO<sub>2</sub> [11] are widely tested. In a substantial number studies commercial Degussa P25 was irradiated in the UV-region [12]. Notably, most of these studied materials are known to absorb only a small amount of photons in the visible range. Moreover, relatively a high recombination rate of the exitons (electron–hole pairs) of the pure polymorph [13] reduces the catalytic efficiency, since corresponding doped materials are known to act as active recombination centers [14]. In search of promising photocatalytic materials mixed binary and ternary oxides of different elements show higher photocatalytic efficiencies at low energy regions, providing an opportunity to use the sunlight [15][16]. But in oxide-based small bandgap semiconductors, the conduction band usually lies at a low level because the deep valence bands are formed by O-2p. This is an underlying major problem for developing photocatalysts functioning in the visible-light range. It is therefore indispensable to tune the valence band with orbitals of other elements instead of O-2p. Bismuth in this regard becomes an established candidate to control the valence band [17]. The 6s of bismuth (d<sup>10</sup>) is susceptible to hybridize O-2p, constituting a shifted/preferable hybridized valence band, which then favors the mobility of photon-induced holes in the valence band and can enhance the photocatalytic performance of the Bi-based oxides. Moreover, the stereochemical activity of 6s<sup>2</sup> lone electron pair was demonstrated playing important roles for the catalytic

enhancement [18]. Studying over a number of Bi-W-oxides it has been found that  $\text{Bi}_2\text{WO}_6$  – the simplest member of the Aurivillius [19] family, exhibits photocatalytic activity under visible light irradiation [20][21][22]. The alternating layers of  $(\text{Bi}_2\text{O}_2)_x$  and  $(\text{WO}_6)_y$  can promote the efficient separation of the exitons. Considering the fact that the photocatalytic activity is inevitably correlated to the average crystallite size, average particle size and particle morphology [21] Zhang et al. [23] demonstrated ultrafine  $\text{Bi}_2\text{WO}_6$  powder to increase the efficiency. Amano et al. [24] showed how the crystalline domains of  $\text{Bi}_2\text{WO}_6$  altered the recombination effects on the photocatalytic activity. In many studies the bandgap, photocatalytic performance are not reported along with the crystal-chemical features of  $\text{Bi}_2\text{WO}_6$ , and discrepancy of the bandgaps between 2.59 eV [20] and 2.9 eV [25] can hardly be justified. The nano-structured phases and morphologies are reported to increase the photocatalytic efficiencies due primarily to specific surface area [26] but, for instance, the bandgap of  $\text{Bi}_2\text{WO}_6$  (2.70, 2.56, 2.67 eV) was not found to be a linear function of the specific surface area ( $20.49$ ,  $25.53$  and  $13.09 \text{ m}^2\cdot\text{g}^{-1}$ , respectively) [23]. Without a complete structural characterization in particular of the nano-crystallites the bandgap value of any photocatalyst seems to be incomplete. Herein we present a detail comparison of the structural and spectroscopic features and the associated bandgaps between quantum dot (QD) ( $< 6 \text{ nm}$ ), nanocrystalline (NC) and polycrystalline (PC) samples of  $\text{Bi}_2\text{WO}_6$  using complementary tools of X-ray powder diffraction (XRPD) followed by Rietveld and pair distribution function (PDF) analysis, transmission electron microscopy (TEM), Raman and UV-Vis spectroscopy as well as density functional theory (DFT).

## **2. Experimental**

### **2.1. Synthesis**

The PC sample was prepared using solid state synthesis. Stoichiometric mixtures of Bi<sub>2</sub>O<sub>3</sub> and WO<sub>3</sub> were grounded under acetone and heated using an alumina crucible for 48 h at 1073 K in air atmosphere with an intermittent grinding after 20 h. The synthesis of NC sample was carried out using a hydrothermal method [27]. Bi(NO<sub>3</sub>)<sub>3</sub>·5H<sub>2</sub>O (98%; Alfa Aesar) and Na<sub>2</sub>WO<sub>4</sub>·2H<sub>2</sub>O (99%; AnalaR NORMAPUR) were dissolved into deionized water followed by putting them in a 50 ml Teflon coated steel autoclave. White precipitates were obtained after a reaction period of 2 hours at 413 K. At room temperature the solid fraction was separated by centrifugation and washed several times with deionized water and finally with anhydrous ethanol (higher solubility regarding NaNO<sub>3</sub>). The material was dried at 353 K for 4 h. The QD sample of Bi<sub>2</sub>WO<sub>6</sub> was synthesized using the flame spray pyrolysis (FSP) method [28][29]. [28,29] Two separate precursor solutions were used. The tungsten precursor was prepared using 3.52 g of tungsten hexacarbonyl (99%; Strem) dissolved in 50 mL THF (99.9%; VWR Chemicals) and gently heated at 313 K. The bismuth precursor contains 12.6 mL bismuth neodecanoate (Sigma-Aldrich) dissolved in 50 mL xylene (98.5%; VWR Chemicals). The metal concentration in each precursor is 0.3 mol/L. The liquid precursors were delivered at a rate of 2.5 mL/min using two syringe pumps (KD Scientific) and mixed prior to the FSP using a T-piece, resulting in an overall precursor flow rate of 5 mL/min. The precursors were atomized by a FSP nozzle using 5 L/min O<sub>2</sub> at a constant pressure drop of 150 kPa at the nozzle tip. The spray was ignited with a supporting CH<sub>4</sub> and O<sub>2</sub> pre-mixed flame (1.5 L/min, 3.2 L/min). The particles were collected 60 cm above the nozzle on a water cooled glass fiber filter (Pall A/E Glass, Ø 25.7 cm) and sieved with a mesh size of 250 µm. Details of the FSP method leading to different particle sizes can be found elsewhere [28][27].

## 2.2. X-ray powder diffraction

Powder diffraction data of the PC sample were collected on a Panalytical X’Pert Pro (Panalytical, Almelo, The Netherlands) in Bragg-Brentano geometry in the range from 5° to

125° 2 Theta with a step width of 0.0167° and a total measurement time of 2 s/step using Ni-filtered CuK<sub>α1,2</sub> radiation ( $\lambda_{\alpha 1} = 154.0598(2)$  pm,  $\lambda_{\alpha 2} = 154.439(1)$  pm, 40 kV, 40 mA). For the NC and QD samples the XRPD data were collected using a StadiP diffractometer (Stoe & Cie, Darmstadt, Germany) with fixed omega scan in the Debye-Scherrer mode, AgK<sub>α1</sub> radiation ( $\lambda = 55.941(1)$  pm, 40 kV, 40 mA), a curved germanium (111) monochromator and a MYTHEN 1K PSD (Dectris, Baden, Switzerland) detector. To get suitable data ( $Q$  above 1 nm<sup>-1</sup>) measurements were carried out with variable counting time [30]. Using 0.015° 2θ data steps the measurement was segmented into 3 slightly overlapping ranges with doubling the counting time in each subsequent higher 2θ range. That is, the measurement from 5° to 53° 2θ was with 150 s/step, 45° to 90° 2θ with 300 s/step and 85° to 126° 2θ with 600 s/step for a period of 2700 s, 5400 s and 10800 s, respectively, for each data set. Rietveld refinements were carried out for the NC and PC data using the Bruker DIFFRAC<sup>plus</sup> TOPAS v4.2 (Bruker AXS Inc., Madison, Wisconsin, USA) software. The crystal data of Bi<sub>2</sub>WO<sub>6</sub> [19] was used as starting model. Instrumental profile parameters [31] were determined for both geometries using a LaB<sub>6</sub>-standard sample. The  $G(r)$  in the PDF analysis describes the probability of finding two atoms separated by a distance of  $r$ . The respective data were refined with an evolutionary algorithm, taking the crystallite-shape into account for the refinement progress of the QD sample. To extract this structure-related information from powder diffraction data the diffraction pattern was background corrected using a separate diffraction measurement of an empty sample container [32]. This corrected X-ray diffraction data were then scaled into electron units and the reduced structure functions [33] are calculated. Finally the structure functions were Fourier transformed to obtain the atomic PDFs (with reduced structure function  $Q[S(Q)-1]$ ) as follows:

$$G(r) = \frac{2}{\pi} \int_{Q=0}^{Q_{max}} Q[S(Q) - 1] \sin(Qr) dQ \quad (1)$$

$$S(Q) = \frac{I^{coh}(Q) - \sum c_i |f_i(Q)|^2}{|\sum c_i f_i(Q)|^2} + 1 \quad (2)$$

The measured three segments were scaled to each other to obtain a continuous data set. These datasets were converted into  $G(r)$  using the PDFgetX3 program [34]. At this point it is important to find the highest  $Q$ -value in the reduced structure function  $F(Q)$  with  $F = 0$ . Otherwise, it would generate Fourier ripples in the  $G(r)$ . At such a point the  $G(r)$  was cut and the remaining data were used for the following structure determination using the program DIFFEV [35]. The program uses a genetic algorithm to optimize the parameters of the bismuth tungstate structure to fit the PDF. A *random particle* was created using DISCUS [36] with the given individual starting parameters. Its theoretical  $G(r)$  is calculated for the resulting residual value. Due to *evolution* of the parameters through the genetic algorithm the refinement was optimized in each generation. The calculations for the individual parameters were performed as given in literature [37] using a Linux cluster (three standard intel i3 computers). By using the program DISCUS and DIFFEV the whole-particle structure of the  $\text{Bi}_2\text{WO}_6$ , lattice parameters, scale-factor, PDF-factors, atomic coordinates and isotropic atomic displacement parameters ( $B$ ) were refined. For the QD sample the particle size was additionally refined.

### **2.3. Spectroscopy**

Raman spectra ( $50 - 2000 \text{ cm}^{-1}$ ) were collected at room temperature on a LabRAM Aramis Raman spectrometer (Horiba/Jobin-Yvon) equipped with a confocal Olympus BX-41 microscope and a CCD detector (Synapse). The measurements were performed using a diffraction grating of 1800 groves/mm, a slit aperture of  $100 \mu\text{m}$  and LASER wavelength of 532 nm.

Solid state UV-VIS absorbance-spectra were collected using a UV-2600 Series spectrometer (Shimadzu) equipped with an ISR-2600Plus two-detector integrating sphere (light source change at 370.0 nm and detector change at 830.0 nm). The Kubelka-Munk transformed data were fitted using a function  $f(\nu)$ . Using the second-derivative of the function we accurately

determined the longest linear part of the raw data, which was fitted using a liner regression. The intercept in the abscissa points to the bandgap. The most commonly used Tauc method [38] cannot directly provide the information on the nature of the transition. To overcome this limitation the derivation of absorption spectrum fitting method (DASF) was demonstrated [39][40].

#### **2.4. Microscopy**

Scanning electron microscopy (SEM) was carried out using a JMS-6510 (JEOL) equipped with an X-Flash 410-M detector (Bruker) for energy dispersive X-ray spectroscopy. A small amount of sample was taken on conducting carbon tabs (mounted on aluminum stubs) and sputtered with gold for 20 s with a JFC-1200 coater (JEOL) followed by inserting them into the SEM chamber. Transmission electron microscopy (TEM) was performed on a Cs corrected TITAN 80/300 (FEI) machine operating at 300 kV. The QD particles were dispersed in ethanol by ultrasonic (400 W) wave and deposited onto a graphene-grid for the measurement.

#### **2.5. Density functional theory (DFT)**

Electronic band structure and density of states were computed using the VASP code [41][42] together with the supplied PAW potentials [43]. An energy cut-off for the plane wave expansion of 560 eV was used as well as a 4x4x4 Monkhorst-Pack grid to sample the full Brillouin zone. We applied the local density approximation for the exchange and correlation part of the potential throughout all DFT computations. The optimized metric parameters ( $a = 549.46(1)$ ,  $b = 1660.33(1)$  pm,  $c = 551.59(1)$  pm) slightly differ from that of the respective experimentally obtained one (see later). Phonon density of states (PDOS) and phonon dispersion were derived using the PHONOPY package [44]. For this purpose a series of 54 supercells (2x1x2) were constructed. In each supercell an atom was displaced as required for the phonon calculations. The forces exerted on each atom caused by the displaced atom are

computed for all supercells in VASP. The resulting sets of forces were then used for the computation of phonons using PHONOPY.

### **3. Results and discussion**

#### ***X-ray diffraction***

X-ray powder data Rietveld refinements showed that the PC and NC possess an average crystallite size of 384(11) nm and 11(1) nm with microstrain of about 5.0(2)% and 2.2(2)%, respectively. The dimension of the QD was found to be about 2.2(1) nm as calculated by PDF. The applied PDF analysis hardly allowed for the calculation of microstrain. Considering the longest lattice parameter of about 1650 pm the QD sample is composed of about only one unit cell along the crystallographic **b**-direction. Figure 1 shows the comparative SEM micrographs between PC, NC and QD samples. The flake-type microstructure is a common feature of the polycrystalline Aurivillius-type materials [45]. The XRPD Rietveld plots of the PC and NC samples are shown in figure 2 and the refined crystal data are given in table 1. The metric parameters of the PC sample agree well with those of the reported ones [19]. Each of the metric parameters of the NC is slightly higher than the respective one of the bulk Bi<sub>2</sub>WO<sub>6</sub> [19]. The *a*- and *c*-cell parameters are equal within the uncertainty (Tab. 1), leading to a pseudo-tetragonal symmetry, whereas the bulk material is orthorhombic with marked difference between *a*- and *c*-cell parameters. It is noteworthy that a decrease in the crystallite size often leads to formation of high-symmetry polymorphs at room temperature, which usually occurs at high temperatures. For instance, it was demonstrated for layered compounds SrBi<sub>2</sub>Ta<sub>2</sub>O<sub>9</sub> [46] and Bi<sub>4</sub>Ti<sub>3</sub>O<sub>12</sub> [47] that the phase-transition temperature decreased with decreasing size of the respective crystallites. It is clear from the comparative powder pattern (Fig. 2) that the QD sample hardly allows for Rietveld analysis due to broad Bragg reflections caused by either small averaged crystallite size or associated microstrain and surface-features. To get real structure both the QD [48] and NC X-ray powder data (Ag-data for higher *Q*-

range only) were investigated using PDF analysis. The PDF data refinement plots are shown in figure 3. The difference curves as well as the  $R_{wp}$  indices ( $R_{wp}(\text{QD}) = 34.41$ ;  $R_{wp}(\text{NC}) = 13.10$ ) indicate that the NC data could be refined with a better convergence. However, the lattice parameters obtained from the PDF analysis are comparable to those obtained from the Rietveld analysis as given in table 2. The QD hardly possess a single unit cell for the calculation of the metric parameters [32]. The PDF analysis allowed for the determination of the average crystallite size and crystallite shape as well as the local geometry of the  $\text{BiO}_x$  and  $\text{WO}_6$  polyhedra, their 3D connectivities and distortions (Tab. 2). The volume of the  $\text{WO}_6$  octahedra slightly decreases from PC to QD. Even in the well crystalline PC the distortion indices (bond length distortion [49], polyhedral mean quadratic elongation [50] and Halasyamani index [51]) of the  $\text{WO}_6$  octahedra are quite high, which increases from PC to NC materials. The  $\text{W}^{6+}(\text{d}^0)$  cation is susceptible to second order Jahn-Teller (SOJT) effects [52], which can be additionally affected by the neighboring  $\text{Bi}^{3+}$  cations with stereochemically active lone electron pairs. The bond valence sum (BVS) [53] of tungsten in both PC and NC lie close to the empirical value. The Bi-atoms are found to be under-bonded (< +3 v.u.) and most of the oxygen atoms are over-bonded (< -2 v.u.). The overall BVS of the atoms in PC is consistent with the measured zeta-potential, demonstrating that the surface is negatively charged as shown in figure 4. For the QD sample the mean BVS of Bi, W and O are found to be +3.3, +5.7 and -1.6 v.u. with respective high uncertainty (which could hardly be given for the mean values), in particular for the atoms sitting close to the surface as shown in figure 5. It is interesting to note that the BVS of the atoms sitting in the inner part of the QD shows close to the respective empirical value whereas the unphysical ones lie only in the surface, which may be due to broken bonds (due lack of lattice translation), grain boundaries and surface-features. Alike NC the QD also possesses dominantly positive charge on the surface; similar zeta potential experiment may cross-check this finding. The stereochemical activity of the  $\text{Bi}^{3+}$  cations in the surface are assumed to be more pronounced than those in the inner bulk

as the BVS is about 0.3 v.u. higher than the empirical value. The averaged high distortion of the  $\text{WO}_6$  may also be related to the surface phenomena of the QD material.

## ***Microscopy***

Due to the fact that like many complex inorganic oxides the dimension of the QD possesses no long-range periodic order, and the crystal structure cannot be solved using conventional X-ray diffraction methods, a complementary TEM and PDF methods allowed for the determination of the correct element ratio and particle/crystallite morphology. Figure 6 shows the high resolution TEM image of the agglomerated particles of the QD. The lattice-plane distances were determined from the grey-scale values of the lattice fringes (Fig. 6). In order to estimate the precision of the lattice-plane distance, the distances corresponding to equivalent reflections have been averaged, yielding a reduced standard deviation. For the investigated area of the TEM image selective distances of 192(2) pm, 272(2) pm, 235.2(3) pm and 317(1) pm were obtained corresponding to the largest lattice-plane distances, which are in good agreement with those obtained from the NC and PC materials as well as the PDF refined structures. Crystallite shapes with morphology were constructed as shown in figure 7; the core of the particle (coordination and their connectivities) was constructed using the  $hkl$  planes obtained from the PDF refinement and the surface morphology from the  $d$ -values obtained from the TEM image. Herein one can verify the results of the PDF refinements regarding the morphology of the average crystallite (Fig. 7) and therefore the whole crystallite refinement is a suitable method to support the TEM investigation of the QD sample.

## ***Vibrational spectroscopy***

Factor group analysis predicts 108 ( $27\text{A}_1 + 27\text{A}_2 + 27\text{B}_1 + 27\text{B}_2$ ) zone center vibrational modes. Of them, 78 ( $26\text{A}_1 + 26\text{B}_1 + 26\text{B}_2$ ) are infrared, 105 ( $26\text{A}_1 + 27\text{A}_2 + 26\text{B}_1 + 26\text{B}_2$ ) are Raman active modes, and ( $\text{A}_1 + \text{B}_1 + \text{B}_2$ ) belongs to acoustic in nature. A detail of the mode analysis was well described elsewhere [54]. Figure 8 shows the Raman spectra of the PC, NC

and QD samples along with the PDOS. The fitted frequencies of PC are in good agreement with those of the reported data [55]. The observed frequencies of NC can be directly comparable to those of the spectrum reported for 9 – 22 nm Bi<sub>2</sub>WO<sub>6</sub> [56]. Compared to the respective phonon frequency the slight red shift of the low frequency modes of NC and QD can be explained in terms of phonon confinement and defects [56]. The Raman spectrum of the QD showed a few broad maxima, which is more or less representative to its phonon density of states (Fig. 8). The low frequency region of the spectral density is comparable to that of the NC sample, however, the high frequency region (600 cm<sup>-1</sup> and 1000 cm<sup>-1</sup>) is significantly shifted to higher energy. The blue shifts observed for the higher frequency region of QD can be explained due to higher distortion of the tungsten octahedra in the samples, caused by significantly larger surface to bulk ratio, and therefore resulting in higher bond strain. Since vibrational spectra are sensitive to particle size [57], shape [45][58], crystallinity and defects/vacancies [59] all of them may be present in the QD sample; a straightforward group theory approach may not predict the accurate frequencies of the optically active modes. Moreover, these factors give rise to broadening and asymmetric line-shapes. Michel et al. [60] documented Raman spectra of some disordered phases showing broad bands, leading to breakdown of the selection rule ( $k = 0$ ) as random distribution of point defects can suppress the translational symmetry, and phonons from all possible parts of the Brillouin zone can contribute to the Raman spectrum. The lattice dynamical properties of the NC and QD can be understood with an adequate knowledge of their bulk counterpart. Raman scattering allows a semi-quantitative measure of the optical branches of the mode frequencies  $\omega_n$  as a function of QD dimension. For this approximation the optical vibrational modes are considered to be confined to the QDs with a spherical geometry, and assigned to an equivalent wavevector [61][62]:

$$k_n = \frac{2\mu_n}{d} \quad (3)$$

where  $\mu_n$  is the  $n$ -th node of the spherical Bessel function  $j_1$  and  $d$  the diameter of the QD. In this macroscopic model a negative bulk LO-phonon dispersion (quadratic) is assumed [61] and the vibrational eigenfrequencies can be obtained as:

$$\omega_n^2 = \omega_L^2 - k_n^2 \beta_L^2 = \omega_L^2 - \left( \frac{2\mu_n \beta_L^2}{d} \right)^2 \quad (4)$$

where  $\omega_L$  is the bulk optical phonon frequency at the Brillouin zone center. Parameter  $\beta_L$  describes the quadratic curvature of the harmonic phonon band restricted to a region close to the zone center as shown in figure 9a. Averaged value of  $\beta_L$  was calculated as 17, 53, 75 and 84 cm<sup>-1</sup>nm of the optical mode of 98, 264, 284 and 306 cm<sup>-1</sup> at the  $\Gamma$ -point by fitting the respective phonon dispersion in the  $\Gamma$ -X,  $\Gamma$ -Y,  $\Gamma$ -T and  $\Gamma$ -R directions. Equation (4) directly relates the size-dependence of the observed optical Raman frequency of the materials. The model line goes through the well resolved low frequency Raman bands of the NC sample as shown in figure 9b. The departure of the model line from the QD data can be explained in terms of the  $\beta_L$  values. That is, the experimental phonon dispersion at ambient conditions the Raman measurements performed at, may be different than those used (calculated at 0 K) for the modeling. Moreover, the frequency resolved for the QD was based on the broad band maxima which may not truly represent the respective Raman frequency.

### **UV-Vis spectroscopy**

The UV-VIS spectra of PC, NC and QD samples of Bi<sub>2</sub>WO<sub>6</sub> along with their respective Tauc [38] and DASF [39] plots are shown in figure 10. The observed and DFT calculated bandgaps are given in table 3. The bandgap calculated by Tauc method (direct) non-linearly differs from that of the DASF method for a given material type. However, the DASF bandgap between PC and NC samples does not significantly differ, which is more or less a representative mean value of most early observations. The DFT bandgap of 1.89(1) eV is comparable to other calculated ones (e.g., 1.63 eV [63], 1.84 eV [18]). The bandgap calculated from DFT differs from the experimental values in two ways. First, the bandgap obtained from the Brillouin

zone center represents the bulk materials. Second, the DFT evaluated bandgap (Tab. 3) is 1 eV less than that of experimentally observed one. It is frequently pointed out as a common feature of DFT calculations [64] that the bandgap calculated by DFT is usually smaller than that of the experimental one. Significantly a higher bandgap of QD can be explained in terms of the incipient separation of  $(\text{Bi}_2\text{O}_3)_x$  from the  $(\text{WO}_6)_y$  layers, where the recombination issue is still an open question. The bandgap of well crystalline PC can be attributed to a charge transition from Bi-6s to W-5d orbitals [65]; a consequence of the independent contributions of the  $(\text{Bi}_2\text{O}_3)_x$  and  $(\text{WO}_6)_y$  layers. In this case the transition of the  $(\text{Bi}_2\text{O}_3)_x$  layer ( $E_g = 2.9$  eV [66]) is comparable to the bandgap of the PC compound.

#### **4. Conclusion**

The structural and the spectroscopic characterizations of the visible light photocatalyst  $\text{Bi}_2\text{WO}_6$  with three different crystallite sizes have been investigated. While the polycrystalline and nanocrystalline samples can be well characterized using conventional X-ray powder diffraction data Rietveld refinement, pair distribution function (PDF) analysis was sought for the structural characterization of the quantum dot (QD) materials. Transmission electron microscopy, Raman spectra and phonon density of states provided complementary aids to understand the structure-property relationship between the materials. There is no significant difference of bandgap between the PC and the NC materials. The higher bandgap of the QD was explained in terms of higher surface/bulk ratio and geometric distortion of the  $\text{BiO}_x$  and  $\text{WO}_6$  polyhedra [67]. An increasing separation between the  $(\text{Bi}_2\text{O}_2)_x$  and  $(\text{WO}_6)_y$  layers was observed, resulting in the observable shift of the bandgap in QDs. This study particularly leaves the message that a true bandgap value of  $\text{Bi}_2\text{WO}_6$  should only be claimed along with its complete structural and morphological signatures.

## Acknowledgement

TMG gratefully acknowledges the Deutsche Forschungsgemeinschaft (DFG) for the financial support in the Heisenberg program (GE1981/3-1 and GE1981/3-2). MT thanks Universität Bremen for the financial support.

## References

- [1] J. Schneider, M. Matsuoka, M. Takeuchi, J. Zhang, Y. Horiuchi, M. Anpo, D.W. Bahnemann, *Chem. Rev.* 114 (2014) 9919.
- [2] H. Ahmad, S.K. Kamarudin, L.J. Minggu, M. Kassim, *Renew. Sustain. Energy Rev.* 43 (2015) 599.
- [3] C.-H. Lee, J.-L. Shie, C.-Y. Tsai, Y.-T. Yang, C.-Y. Chang, *J. Clean Energy Technol.* 1 (2013) 115.
- [4] M.M. Haque, D. Bahnemann, M. Muneer, *Photocatalytic Degrad. Org. Pollut. Mech. Kinet.* 3 (2012) 294.
- [5] H. Zangeneh, A.A.L. Zinatizadeh, M. Habibi, M. Akia, M. Hasnain Isa, *J. Ind. Eng. Chem.* 26 (2015) 1.
- [6] A. Fujishima, K. Honda, *Nature* 238 (1972) 37.
- [7] H. Kisch, *Angew. Chemie - Int. Ed.* 52 (2013) 812.
- [8] E.P. Melián, C.R. López, A.O. Méndez, O.G. Díaz, M.N. Suárez, J.M. Doña Rodríguez, J.A. Navío, D. Fernández Hevia, *Int. J. Hydrogen Energy* 38 (2013) 11737.
- [9] K. Nakata, A. Fujishima, *J. Photochem. Photobiol. C Photochem. Rev.* 13 (2012) 169.
- [10] W. Yan, B. Chen, S.M. Mahurin, V. Schwartz, D.R. Mullins, a R. Lupini, S.J. Pennycook, S. Dai, S.H. Overbury, *J. Phys. Chem. B* 109 (2005) 10676.
- [11] Z. Zhang, C.-C. Wang, R. Zakaria, J.Y. Ying, *J. Phys. Chem. B* 102 (1998) 10871.
- [12] T. Ohno, K. Sarukawa, K. Tokieda, M. Matsumura, *J. Catal.* 203 (2001) 82.
- [13] R. Kaplan, B. Erjavec, A. Pintar, *Appl. Catal. A Gen.* 489 (2015) 51.
- [14] M.D. Hernández-Alonso, F. Fresno, S. Suárez, J.M. Coronado, *Energy Environ. Sci.* 2 (2009) 1231.
- [15] A. Di Paola, E. García-López, G. Marcì, L. Palmisano, *J. Hazard. Mater.* 211–212 (2012) 3.
- [16] S. Suib, ed., *New and Future Developments in Catalysis*, First Edit, Elsevier B.V., 2013.
- [17] A. Kudo, K. Omori, H. Kato, *J. Am. Chem. Soc.* 121 (1999) 11459.
- [18] F. Ren, J. Zhang, Y. Wang, *RSC Adv.* 5 (2015) 29058.
- [19] K.S. Knight, *Mineral. Mag.* 56 (1992) 399.

## Journal of Solid State Chemistry

---

- [20] A.P. Finlayson, V.N. Tsaneva, L. Lyons, M. Clark, B.A. Glowacki, *Phys. Status Solidi Appl. Mater. Sci.* 203 (2006) 327.
- [21] M. Shang, W. Wang, S. Sun, L. Zhou, L. Zhang, *J. Phys. Chem. C* 112 (2008) 10407.
- [22] L. Zhang, D. Bahnemann, *ChemSusChem* 6 (2013) 283.
- [23] Z. Zhang, W. Wang, M. Shang, W. Yin, *J. Hazard. Mater.* 177 (2010) 1013.
- [24] F. Amano, A. Yamakata, K. Nogami, M. Osawa, B. Ohtani, *J. Am. Chem. Soc.* 130 (2008) 17650.
- [25] Y. Zhou, Y. Zhang, M. Lin, J. Long, Z. Zhang, H. Lin, J.C.-S. Wu, X. Wang, *Nat. Commun.* 6 (2015) 8340.
- [26] D. Nagy, T. Firkala, X. Fan, I.M. Szilágyi, *Eur. Chem. Bull.* 5 (2016) 40.
- [27] X. Gao, W. Li, F. Fu, Y. Wu, D. Li, J. Wang, *China Pet. Process. Petrochemical Technol.* 13 (2011) 19.
- [28] L. Mädler, H.K. Kammler, R. Mueller, S.E. Pratsinis, *J. Aerosol Sci.* 33 (2002) 369.
- [29] W.Y. Teoh, R. Amal, L. Mädler, *Nanoscale* 2 (2010) 1324.
- [30] I.C. Madsen, R.J. Hill, *IUCr, J. Appl. Crystallogr.* 27 (1994) 385.
- [31] A.A. Coelho, J. Evans, I. Evans, A. Kern, S. Parsons, *Powder Diffr.* 26 (2011) S22.
- [32] S.J.L.B. T. Egami, *Underneath the Bragg Peaks*, Pergamon, 2003.
- [33] H.P. Klug, L.E. Alexander, *X-Ray Diffraction Procedures: For Polycrystalline and Amorphous Materials*, second, Wiley, 1974.
- [34] P. Juhás, T. Davis, C.L. Farrow, S.J.L. Billinge, *J. Appl. Crystallogr.* 46 (2013) 560.
- [35] K. Page, T.C. Hood, T. Proffen, R.B. Neder, *J. Appl. Crystallogr.* 44 (2011) 327.
- [36] T. Proffen, R.B. Neder, *J. Appl. Crystallogr.* 30 (1997) 171.
- [37] S. Gotshall, B. Rylander, *Proc. Genet. Evol. Comput. Conf.* (2000) 1.
- [38] J. Tauc, *Mater. Res. Bull.* 3 (1968) 37.
- [39] D. Souri, Z.E. Tahan, *Appl. Phys. B Lasers Opt.* 119 (2015) 273.
- [40] A. Kirsch, M.M. Murshed, M. Schowalter, A. Rosenauer, T.M. Gesing, *J. Phys. Chem. C* 120 (2016) 18831.
- [41] G. Kresse, J. Hafner, *Phys. Rev. B* 47 (1993) 558.
- [42] G. Kresse, J. Furthmüller, *Comput. Mater. Sci.* 6 (1996) 15.
- [43] G. Kresse, *Phys. Rev. B* 59 (1999) 1758.
- [44] A. Togo, I. Tanaka, *Scr. Mater.* 108 (2015) 1.
- [45] L. Zhang, H. Wang, Z. Chen, P.K. Wong, J. Liu, *Appl. Catal. B Environ.* 106 (2011) 1.

- [46] T. Yu, Z.X. Shen, W.S. Toh, J.M. Xue, J. Wang, *J. Appl. Phys.* 94 (2003) 618.
- [47] Y.L. Du, M.S. Zhang, Q. Chen, Z. Yin, *Appl. Phys. A Mater. Sci. Process.* 76 (2003) 1099.
- [48] S.J.L. Billinge, M.G. Kanatzidis, *Chem. Commun.* (2004) 749.
- [49] W.H. Baur, *Acta Crystallogr. Sect. B Struct. Crystallogr. Cryst. Chem.* 30 (1974) 1195.
- [50] K. Robinson, G. V. Gibbs, P.H. Ribbe, *Science* (80- ). 172 (1971) 567.
- [51] P.S. Halasyamani, *Chem. Mater.* 16 (2004) 3586.
- [52] M. Kunz, I.D. Brown, *J. Solid State Chem.* 115 (1995) 395.
- [53] N.E. Brese, M. O'Keeffe, *Acta Crystallogr. B* 47 (1991) 192.
- [54] H.C. Gupta, Archana, V. Luthra, *J. Mol. Struct.* 1005 (2011) 53.
- [55] M. Maczka, J. Hanuza, W. Paraguassu, A. Gomes Souza Filho, P. Tarso Cavalcante Freire, J. Mendes Filho, *Appl. Phys. Lett.* 92 (2008) 112911.
- [56] M. Mączka, L. Macalik, K. Hermanowicz, L. Kępiński, P. Tomaszewski, *J. Raman Spectrosc.* 41 (2010) 1059.
- [57] J.E. Spanier, R.D. Robinson, F. Zhang, S.-W. Chan, I.P. Herman, *Phys. Rev. B* 64 (2001) 245407.
- [58] C. Burda, X. Chen, R. Narayanan, M.A. El-Sayed, *Chem. Rev.* 105 (2005) 1025.
- [59] W.B. Keramidas, V.G. Whites, *J.Phys.Chem.Solids* 34 (1973) 1873.
- [60] D. Michel, R. Collongues, *J. Raman Spectrosc.* 5 (1976) 163.
- [61] E. Roca, C. Trallero-Giner, M. Cardona, *Phys. Rev. B* 49 (1994) 13704.
- [62] C. Trallero-Giner, A. Debernardi, M. Cardona, E. Menéndez-Proupín, A. Ekimov, *Phys. Rev. B* 57 (1998) 4664.
- [63] H. Fu, C. Pan, W. Yao, Y. Zhu, *J. Phys. Chem. B* 109 (2005) 22432.
- [64] R.M. Dreizler, E.K. Gross, *Density Functional Theory: An Approach to the Quantum Many-Body Problem*, Springer-Verlag, Berlin, 1990.
- [65] H. Yamashita, Hiromi, Li, ed., *Nanostructured Photocatalysts: Advanced Functional Materials*, First, Springer International Switzerland, 2016.
- [66] Y.A. Shaban, S.U.M. Khan, *Int. J. Photoenergy* 2012 (2012).
- [67] G. Wijs, P. Boer, R. Groot, G. Kresse, *Phys. Rev. B* 59 (1999) 2684.

**Tables and figures**

**Table 1:** Rietveld refined parameters obtained from the X-ray powder data of the polycrystalline (PC; CuK $\alpha$ 1,2;  $\lambda = 154.059(1)$  pm) and nanocrystalline (NC; AgK $\alpha$ ;  $\lambda = 55.941(1)$  pm) samples of Bi<sub>2</sub>WO<sub>6</sub>.

Sample PC, <i>Pca2<sub>1</sub></i> , $a = 543.6974(40)$ pm, $b = 1643.513(12)$ pm, $c = 545.7827(40)$ pm, $R_{wp} = 8.96$						
Atom	Site	Occupancy	<i>x</i>	<i>y</i>	<i>z</i>	$B / \text{pm}^2 \cdot 10^4$
Bi1	4a	1	0.52063(51)	0.42299(18)	0.97661(86)	0.33(70)
Bi2	4a	1	0.48340(33)	0.07740(12)	0.98034(88)	0.52(79)
W1	4a	1	0.00773(70)	0.25027(36)	0.00000(0)	0.13(80)
O1	4a	1	0.05884(78)	0.14102(30)	0.07758(90)	0.95(90)
O2	4a	1	0.26021(58)	0.99981(26)	0.26425(97)	1.24(87)
O3	4a	1	0.24091(46)	0.50134(26)	0.25850(70)	0.56(98)
O4	4a	1	0.70664(68)	0.23263(16)	0.25167(83)	1.23(42)
O5	4a	1	0.21322(55)	0.26461(26)	0.33174(90)	1.02(71)
O6	4a	1	0.56231(80)	0.35994(33)	0.56187(89)	1.09(78)

Sample NC, <i>Pca2<sub>1</sub></i> , $a = 545.61(20)$ pm, $b = 1641.46(5)$ pm, $c = 545.60(20)$ pm, $R_{wp} = 6.05$						
Atom	Site	Occupancy	<i>x</i>	<i>y</i>	<i>z</i>	$B / \text{pm}^2 \cdot 10^4$
Bi1	4a	1	0.5206(3)	0.4224(1)	0.9761(5)	0.18(4)
Bi2	4a	1	0.4824(3)	0.0771(1)	0.9796(5)	0.36(4)
W1	4a	1	0.0071(8)	0.2495(2)	0	0.10(1)
O1	4a	1	0.0579(7)	0.1402(2)	0.0768(7)	0.85(7)
O2	4a	1	0.2597(3)	0.9994(2)	0.2635(8)	0.69(8)
O3	4a	1	0.2403(3)	0.5006(2)	0.2576(9)	0.40(7)
O4	4a	1	0.7059(4)	0.2324(1)	0.2507(5)	0.79(3)
O5	4a	1	0.2131(4)	0.2639(1)	0.3308(5)	0.96(3)
O6	4a	1	0.5616(7)	0.3598(2)	0.5618(6)	0.70(8)

**Table 2.** Crystal structure parameters obtained from the X-ray data Rietveld refinements and pair distribution function (PDF) analyses between polycrystalline (PC), nanocrystalline (NC) and quantum dot (QD) samples of  $\text{Bi}_2\text{WO}_6$ .

Parameter	PC (Rietveld)	NC (Rietveld)	NC (PDF)	QD (PDF)
$a$ /pm	543.6974(40)	545.61(20)	544.503(30)	-
$b$ /pm	1643.513(12)	1641.46(5)	1634.320(60)	-
$c$ / pm	545.7827(40)	545.60(20)	543.291(40)	-
$V/10^6 \cdot \text{pm}^3$	487,6970	488,6377	483,47039	-
<b>WO<sub>6</sub> geometry and distortions</b>				
W-O dist. /pm	193.93(7)	194.17(6)	188.52(8)	191.53(2)
WO <sub>6</sub> vol. /10 <sup>6</sup> ·pm <sup>3</sup>	9.44(3)	9.49(2)	8.42(3)	8.29(3)
$\lambda_d$ /%	7.211(4)	7.079(5)	11.63(1)	8.44(1)
$\lambda_{\text{oct}}$ /%	1.02(5)	2.49(6)	5.62(2)	9.47(1)
$\Delta_d$ /pm	0.70(1)	0.71(1)	1.03(1)	1.72(2)

$\lambda_d$  = bond length distortion,  $\lambda_{\text{oct}}$  = octahedral mean quadratic elongation;  $\Delta_d$  = Halasyamani distortion index.

**Table 3:** Calculated and experimental values of electronic bandgaps of polycrystalline (PC), nanocrystalline (NC) and quantum dot (QD) samples of  $\text{Bi}_2\text{WO}_6$ .

Sample type	Bandgap /eV (Tauc)	Bandgap /eV (DASF)	Bandgap /eV (DFT)
PC	2.71(7)	2.87(7)	1.89(1)*
NC	3.09(4)	2.78(4)	-
QD	2.87(4)	2.98(7)	-

DASF = derivation of absorption spectrum fitting (also see [39] & [40])

\*value represents bulk material or PC.

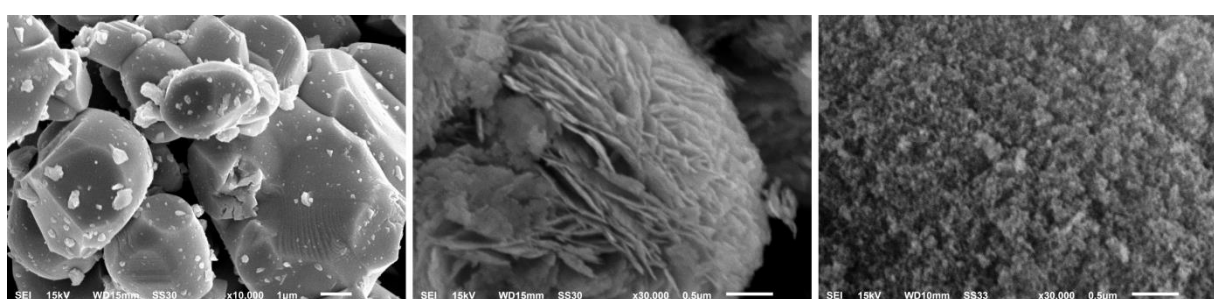


**Figure 1:** Scanning electron micrographs of polycrystalline (PC, left), nanocrystalline (NC, middle) and quantum dot (QD, right) samples of  $\text{Bi}_2\text{WO}_6$ .

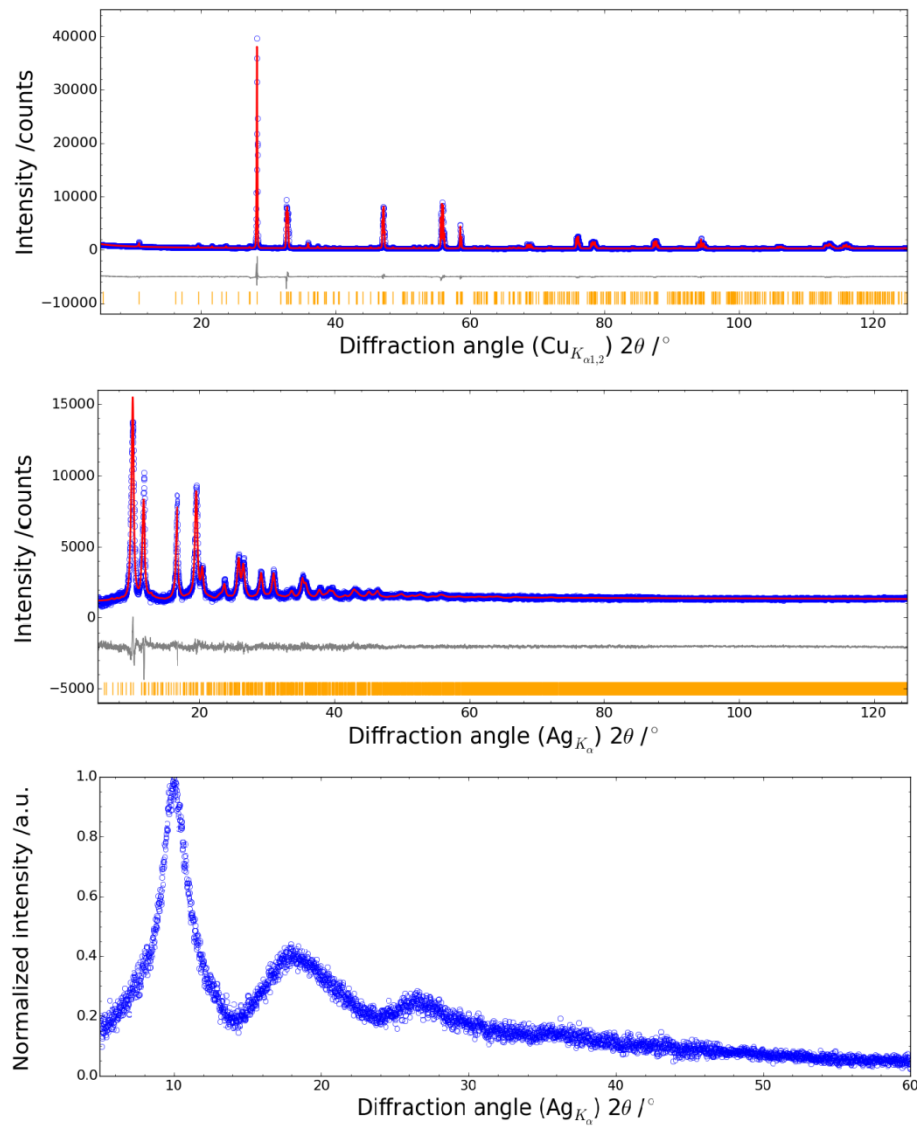


**Figure 2:** Rietveld plots of the polycrystalline (PC, top), nanocrystalline (NC, middle) and X-ray powder diffraction patterns of the quantum dot (QD, bottom) samples of  $\text{Bi}_2\text{WO}_6$ .

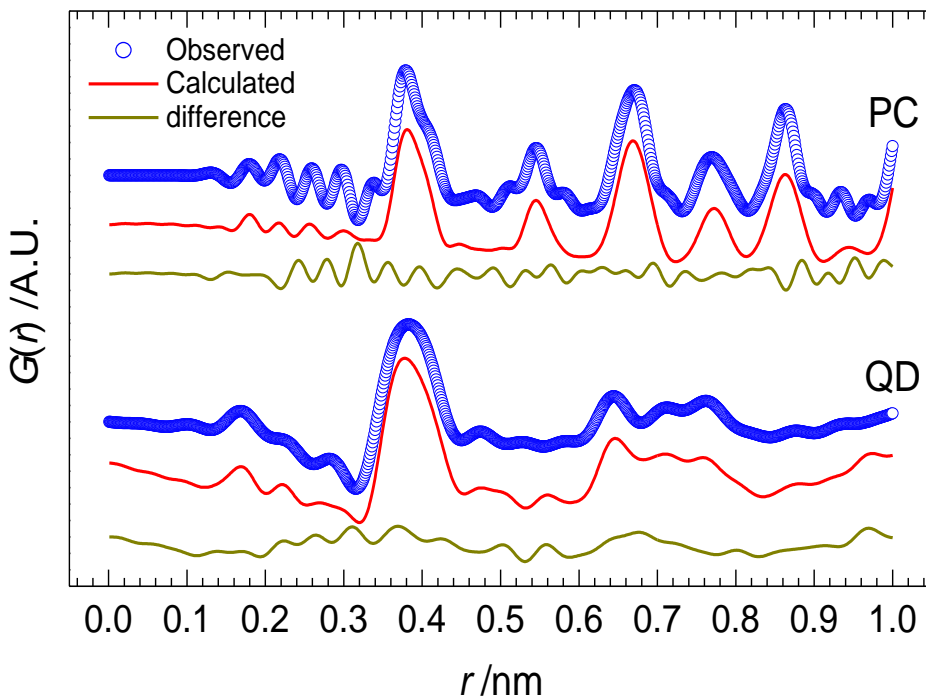


**Figure 3:** Pair distribution function data refinement plots of the nanocrystalline (NC) and quantum dot (QD) samples of  $\text{Bi}_2\text{WO}_6$ .

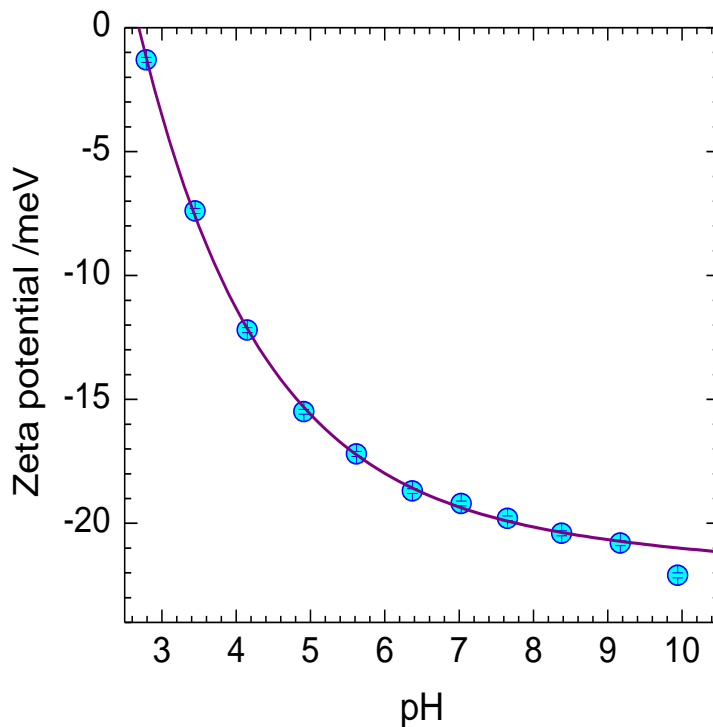


**Figure 4:** pH-dependent zeta-potential of the nanocrystalline (NC)  $\text{Bi}_2\text{WO}_6$  sample. The solid line is for eye guideline.

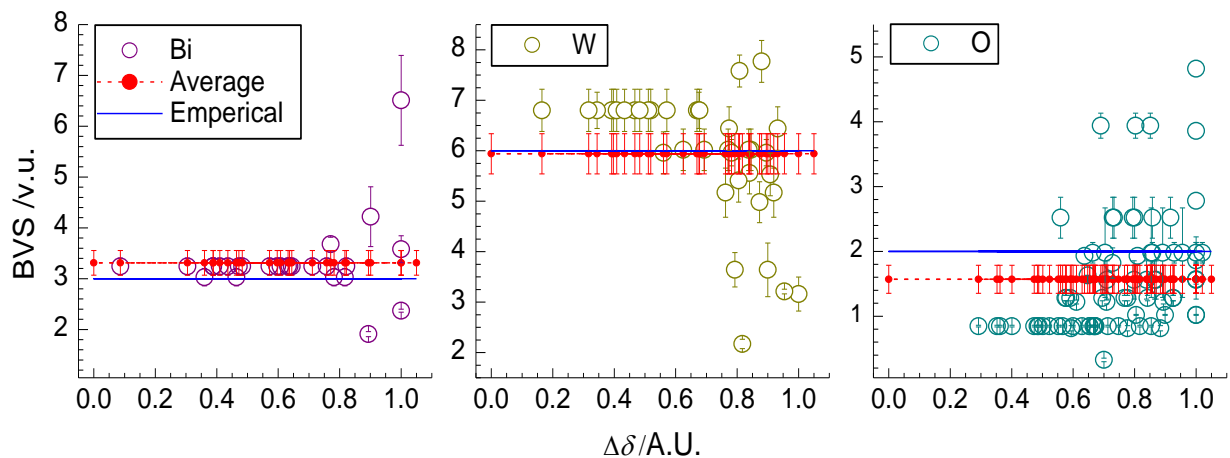


**Figure 5:** Change of the absolute value of the bond valence sum (BVS) of bismuth (left), tungsten (middle) and oxygen (right) from core (0) to the surface of the quantum dot (QD) sample of Bi<sub>2</sub>WO<sub>6</sub>.

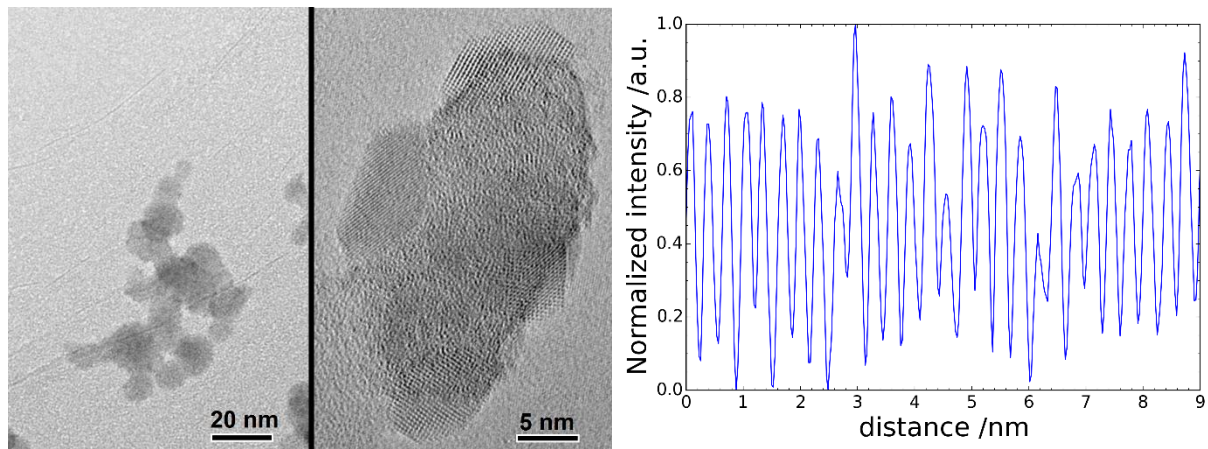


**Figure 6:** TEM images of quantum dot Bi<sub>2</sub>WO<sub>6</sub> sample (left) along with the lattice-plane distances obtained from the grey-scale values of the lattice fringes.

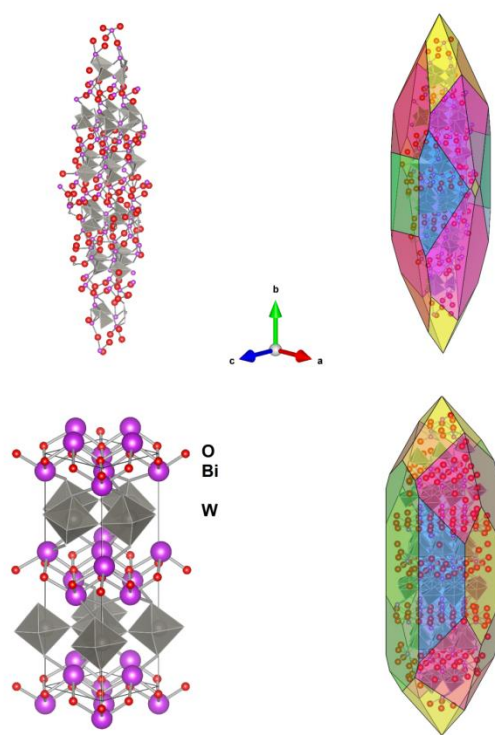


**Figure 7:** The average whole particle structure and shape constructed from the PDF data refinement (top). The outer-planes of the particle were constructed from the  $d$ -values of the TEM fringes. The crystal structure of the nanocrystalline (NC, bottom)  $\text{Bi}_2\text{WO}_6$  sample along with a constructed particle using multiple unit cells.

**Figure 8:** Raman spectra of polycrystalline (PC), nano-crystalline (NC) and quantum dot (QD) of  $\text{Bi}_2\text{WO}_6$  samples. The vertical bars show the respective mode frequencies of the present study as well as theoretical values ([54][55]).

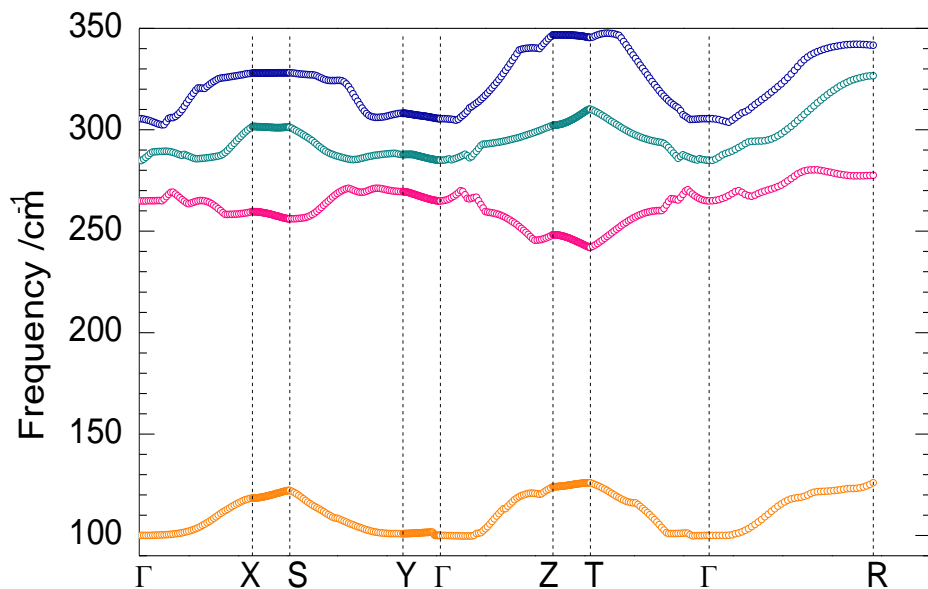


**Figure 9a:** Selective phonon dispersion of  $\text{Bi}_2\text{WO}_6$  along some high-symmetry directions.

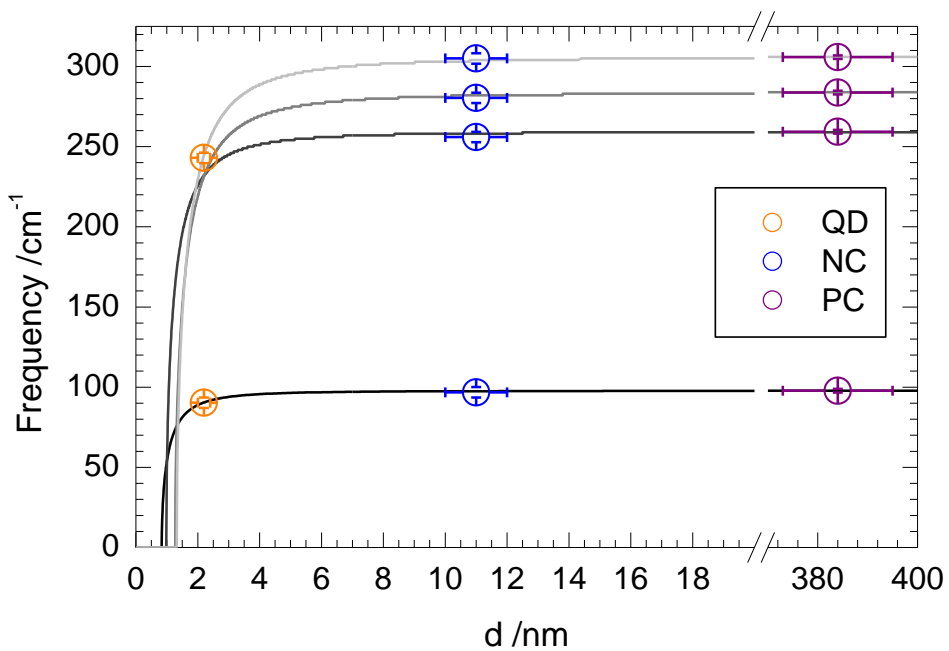


**Figure 9b:** Radial dependence of the optical vibrational energies of the spherical polycrystalline (PC), nanocrystalline (NC) and the quantum dot (QD) samples of  $\text{Bi}_2\text{WO}_6$  as a function of particle diameter ( $d$ ). Each solid line refers to model fit.

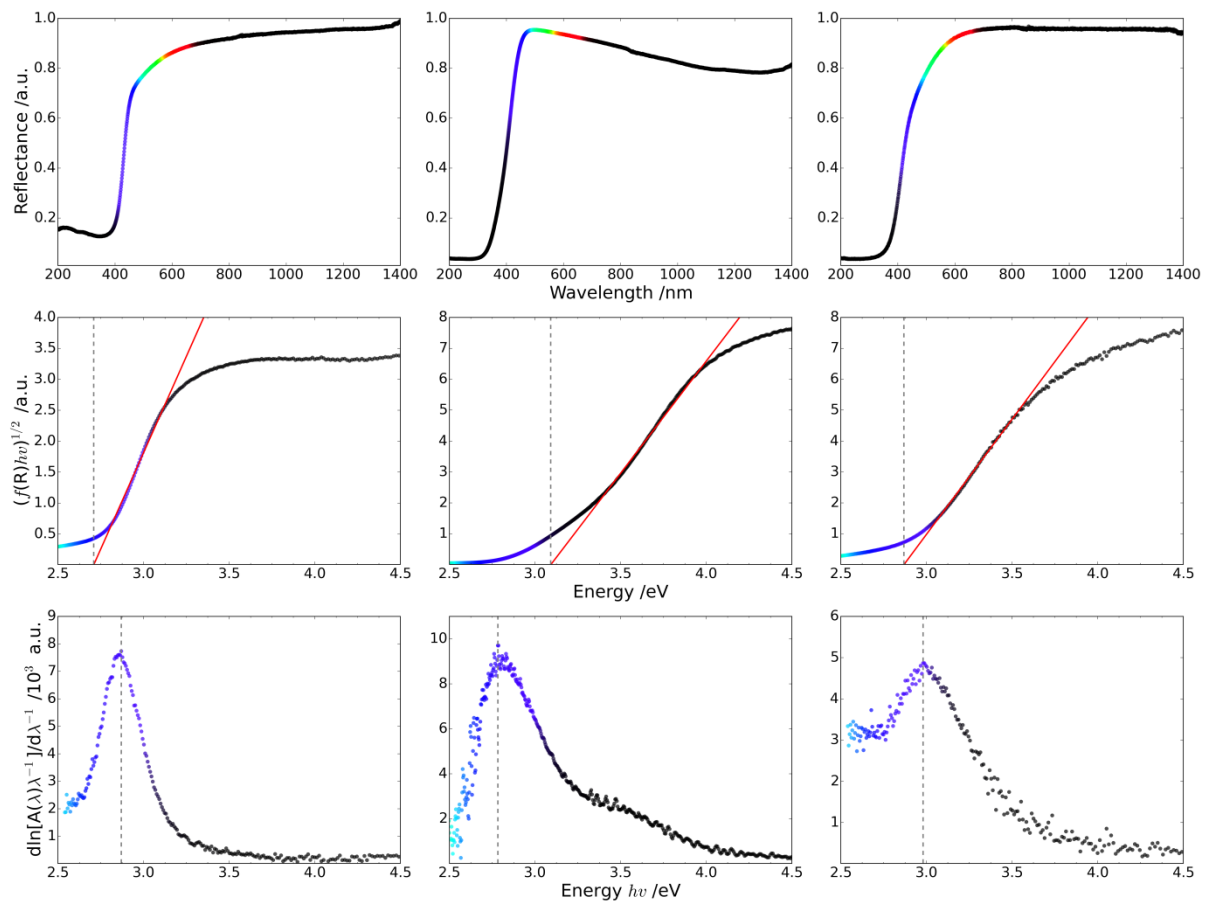


**Figure 10:** UV/Vis absorbance spectra (top), Tauc (middle) and DASF (bottom) plots of the polycrystalline (PC), nanocrystalline (NC) and the quantum dot (QD) samples of  $\text{Bi}_2\text{WO}_6$ . The solid lines elsewhere show the fitted lines/peaks and the dotted lines the bandgaps.